Faraday Discussions

Cite this: *Faraday Discuss.*, 2020, **221**, 245

PAPER

Exploring the capabilities of optical pump X-ray probe NEXAFS spectroscopy to track photo-induced dynamics mediated by conical intersections

Francesco Segatta, †*[a] Artur Nenov, †*[a] Silvia Orlandi, [a] Alberto Arcioni, [a] Shaul Mukamel [b] and Marco Garavelli *[a]

Received 23rd May 2019, Accepted 1st July 2019
DOI: 10.1039/c9fd00073a

X-ray spectroscopy is gaining a growing interest in the scientific community, as it represents a versatile and powerful experimental toolbox for probing the dynamics of both core and valence electronic excitations, nuclear motions and material structure, with element and site specificity. Among the various X-ray based techniques, near-edge X-ray absorption fine structure (NEXAFS) spectroscopy, which investigates the energy and probability of resonant core-to-valence transitions, has started to be applied to organic molecules: a recent UV-pump X-ray probe time-resolved NEXAFS experiment [Wolf *et al.*, *Nat. Commun.*, 2017, **8**, 1] has shown the capability of the technique to provide information about the ultrafast internal conversion between the bright ππ* and the dark nπ* electronic states of the nucleobase thymine. In the present contribution we introduce an accurate theoretical approach for the simulation of NEXAFS spectra of organic molecules, employing azobenzene as a test case. The electronic structure calculations, which provide both energy levels and transition probabilities of core-to-valence excitations, were here performed with a high level multiconfigurational method, the restricted active space self consistent field (RASSCF/RASPT2). GS- and nπ*-NEXAFS spectra were obtained on the top of key molecular geometries (as the optimized *cis*, *trans* and conical intersection(s) structures) as well as along the fundamental isomerization coordinates (namely, symmetric and asymmetric bendings of the phenyl rings, and torsion around the central dihedral). We eventually characterize and explain the origin of the simulated signals, highlighting the specific signatures that make it possible to follow the excited state evolution from the nπ* Franck–Condon point, towards the conical intersection(s).

[a]*Dipartimento di Chimica Industriale "Toso Montanari", Università degli studi di Bologna, Viale del Risorgimento 4, 40136 Bologna, Italy. E-mail: francesco.segatta2@unibo.it; artur.nenov@unibo.it; marco.garavelli@unibo.it*

[b]*Department of Chemistry and Physics and Astronomy, University of California, Irvine, CA 92697, USA*

† These authors contributed equally to this work.

1 Introduction

Photoinduced nonadiabatic phenomena in molecules and supramolecular assemblies are ubiquitous. Conical intersections (CIs) open the door to ultrafast (sub-100 fs) nonradiative internal conversion between electronic states of the same spin multiplicity, controlling product yields and rates in virtually all photochemical and photophysical processes. Recent developments in multidimensional electronic spectroscopy, giving access to unprecedented short laser pulses with remarkable phase stability, have overcome the limitations of spectral congestion and low temporal resolution. This technical progress has provided the tools required to follow the ultrafast dynamics of molecular systems and holds the promise to reveal direct unambiguous fingerprints of the passage through a CI. The increasing complexity of the spectroscopic techniques gives rise to equally complex spectral signatures, whose direct interpretation is often hard or impossible. To disentangle all measured features and draw a detailed and reliable map of the energy transfer routes, it is therefore mandatory to support experimental measurements with theoretical models relying on a unified and fully integrated experimental-computational approach. Such an integrated approach has become paramount in the analysis and interpretation of transient optical spectroscopies, spanning the IR-VIS-UV spectral window. The development of X-ray free-electron laser facilities[1–3] paves the way to extend this approach to the rapidly growing field of novel multidimensional nonlinear spectroscopic techniques, ranging from X-ray stimulated Raman[4] to time-resolved X-ray diffraction.[5]

X-ray spectroscopy provides a complementary tool for tracking of molecular excited state dynamics with respect to the more widely employed optical spectroscopy. Besides the improved temporal resolution which can be pushed down to the attosecond time scale, X-ray techniques are aspired to because of their element- and site-selectivity: they allow spectroscopically different elements to be distinguished even within the same molecule due to the strong difference in the binding energy of core electrons ($\sim$100 eV difference for C, N and O). The subtle sensitivity of the binding energies to the composition of the immediate surroundings makes X-rays another promising tool for structural analysis[6] and for probing molecular dynamics.

Several X-ray techniques for tracking excited state molecular dynamics have emerged in the recent years.[7] In all such experiments, the photoactive molecule is initially excited by means of an optical pulse, populating a valence electronic state, and the excited state electronic structure is then probed by a delayed soft X-ray pulse. Near-edge X-ray absorption fine structure (NEXAFS) spectroscopy is used to probe resonant core-to-valence excitations.[8] In X-ray photoelectron emission (XPS), X-rays are used to eject a core electron from the molecule whose kinetic energy is recorded. Finally, X-ray emission spectroscopy (XES) studies the characteristic wavelengths of photons emitted by valence electrons when filling a previously generated core hole, a process known as Auger decay.[9]

The above techniques have been successfully applied in the transient X-ray spectroscopy of transition metal-based compounds.[9–11] More recently, applications to photo-energy and internal conversion in organic molecules have been reported.[12,13] In particular, the authors of ref. 13 investigated the $\pi\pi^*$ to $n\pi^*$ internal conversion in thymine by means of time-resolved NEXAFS. Wolf and co-

workers exploited the fact that excitations from the thymine oxygen core can be promoted not only to unoccupied valence orbitals, but also to formerly occupied orbitals (of n and π character) in which the preceding optical excitation has created a hole. Moreover, the core-to-n transition was demonstrated to have high oscillator strength. Thus, the formation of the hole in the n orbital during $\pi\pi^*$ to $n\pi^*$ internal conversion was detected as a clear resonance below the K-edge in the absorption spectrum of the oxygen, thereby demonstrating the sensitivity of the technique to capture the ultrafast $\pi\pi^*$ to $n\pi^*$ internal conversion (on a sub-ps time scale).

In this contribution we extend the idea and explore, by means of theoretical simulations, the sensitivity of optical pump near-edge X-ray probe spectroscopy to photoinduced excited state dynamics in conjugated organic molecules containing heteroatoms with electron lone pairs. By means of the multiconfigurational restricted active space self consistent field (RASSCF) approach[14] corrected by second order perturbation (RASPT2)[15,16] we simulate NEXAFS spectra of azobenzene probing the ground state (GS) and the $n\pi^*$ excited state at representative molecular geometries. Recently, Ehlert *et al.* published a theoretical study of the GS-, $n\pi^*$- and the $\pi\pi^*$-NEXAFS spectra of *trans*- and *cis*-azobenzene performed within the framework of density functional theory (DFT).[17] Our study extends beyond the Franck–Condon (FC) points and covers the entire isomerization pathway connecting the *trans*- and the *cis*-forms. Furthermore, we derive a simple orbital-based model which successfully rationalizes the observed spectral shifts and line shapes.

Our simulations reveal characteristic signal trends along key modes involved in the isomerization of azobenzene, *i.e.* torsion and bending. We note, however, that the documented trends are generally valid for any *cis–trans* isomerization reaction. While in conventional (optical) spectroscopy techniques the evidence of passage through a crossing region is merely extrapolated (due to extremely red-shifted signals and cancellation of their oscillator strength[18]), here we demonstrate a clear indication of a system evolution towards and through the CI which can be directly observed with X-ray techniques provided they have the required temporal resolution.

Finally, we discuss the transferability of the findings to other systems for which the here observed NEXAFS features can be exploited to track their photoinduced dynamics and to pinpoint in time the passage through the CI. In summary, we expect organic molecules containing heteroatoms with electron lone pairs (like nucleobases, amino acids, and more general azoswitches) and exhibiting a ballistic motion of the excited state wave packet towards the CI, to be good candidates for a clean time-resolved mapping of the excited state potential energy surface with the already available X-ray techniques.

2 Computational details

Core excitations in molecular systems absorb above a few hundreds of eV and are thus preceded by a vast number of valence states. Therefore, a strategy is required to target specifically desired core excitations. The restricted active space self consistent field (RASSCF) approach[14] from the family of multi-configuration wavefunction-based methods offers a neat way to cope with this issue. In a RASSCF calculation the active space, *i.e.* the list of orbitals and electrons of

paramount importance for describing the electronic structure of the system, is divided into subspaces: RAS1 with an upper limit of holes; RAS2 where all permutations of electrons within the orbitals are considered; RAS3 with a maximal number of simultaneously excited electrons. In this regard, RASSCF offers a higher flexibility with respect to the more commonly used complete active space approach (CASSCF) which does not distinguish between subspaces,[19,20] thus effectively removing "dead wood" from the list of configuration state functions (CSFs) without sacrificing accuracy. The missing (dynamical) correlation can be added on top of a RASSCF calculation through second-order perturbation (RASPT2).[15,16,21]

A common strategy to treat core–valence excitations within the RASSCF/RASPT2 framework is to place the core orbital(s) in RAS3 and use an upper limit of $n - 1$ electrons into this subspace with n being the total number of electrons in the fully occupied core orbital(s). Thereby, the list of CSFs is forced to include only core-hole configurations. This strategy has been applied to compute near-edge X-ray spectroscopy of metal complexes[22,23] as well as X-ray Raman of organic compounds.[24] A considerable drawback of this approach is that the core–valence transition dipole moments are not straightforwardly accessible due to the fact that valence and core-hole states need to be computed with different RAS3 limits for maximal occupation (n for valence states, $n - 1$ for core-hole states).

Here we utilize a different approach, based on a novel projection technique recently implemented in OpenMolcas,[25] called highly excited states (HEXS) which sets to zero the CI coefficients of all CSFs with the maximum occupation from a given subspace, thus effectively projecting them out of the wavefunction.[26] The HEXS approach allows the transition dipole moments of the core-excited states to be modelled. Furthermore, the HEXS technique allows mixed core-excitations to be handled, *e.g.* by placing different core orbitals in RAS1 and RAS2 and applying the projector operator to both, and can be straightforwardly extended to multiple core excitations.[26] This offers intriguing possibilities in combination with the generalized version of the RASSCF technique, known as GASSCF,[27,28] which removes the restriction of working with only three subspaces. Applications of the HEXS technique can be found in ref. 22, 29 and 30.

In the following we outline the protocol for computing the nitrogen near-edge X-ray spectra in azobenzene:

(1) A Hartree–Fock calculation is performed which is used to construct the active space; due to the symmetry of azobenzene the canonical nitrogen core orbitals are delocalized; in order to calculate contributions from individual cores, core-localized orbitals are obtained by linear combination;

(2) The active space is constructed as follows (see Fig. 1):

- RAS1: one core orbital is placed herein and kept frozen to avoid orbital rotation (using the SUPSYM keyword); the upper limit of holes was set to 1;
- RAS2: all occupied valence π- and n-type orbitals were placed herein;
- RAS3: all virtual valence π^*-type orbitals were placed herein and an upper limit of 4 excitations was set;

In the following we designate the active space as RAS(1, 1|18, 9|4, 7), where the first pair of indices denote the upper limit of holes and the number of orbitals in RAS1, the second pair the number of electrons and orbitals in RAS2, and the third pair the upper limit of excitations and the number of orbitals in RAS3;

(3) RASSCF calculations were performed separately:

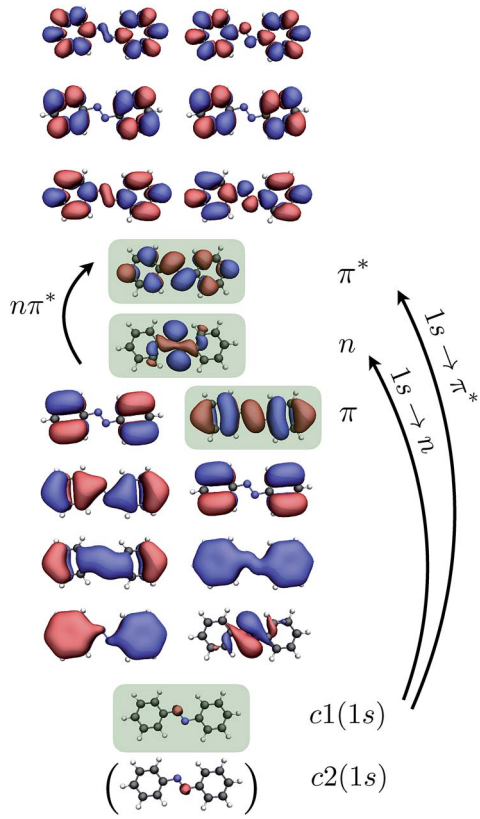

Fig. 1 Active space (in order of the orbital occupation) of the SA-2-RASSCF(1, 1|18, 9|4, 7) *trans*-azobenzene valence states computation and diagram of the transitions relevant to this work. Key orbitals are highlighted in green colored boxes. If not otherwise specified, the nitrogen lone pair n and the π* orbital refer to, respectively, the highest occupied and the lowest unoccupied orbitals. The two core orbitals are denoted with the labels c1 and c2. The orbitals were drawn employing VMD.[31,32]

• For the valence states, where up to two states (GS and nπ* states) were included in the state-averaging, *i.e.* SA-2-RASSCF(1, 1|18, 9|4, 7). Around 90° torsion, state average over three roots (given through one open shell and two closed shell configurations in the frontier localized orbitals) allows for a more equilibrate description of the electronic structure. Due to the energetic proximity of the involved states we applied the multi-state (MS) version of RASPT2 which reduces wavefunction mixing;

• For each of the two nitrogen core-orbitals, where the HEXS keyword was utilized to force the creation of the core hole, and up to 15 states were included in the state-averaging, *i.e.* SA-15-core-RASSCF(1, 1|18, 9|4, 7); in structures exhibiting symmetry with respect to the nitrogen core-orbitals it is sufficient to perform the computations accounting for only one of the two cores.

(4) Unless specified otherwise in the text, single state (SS)-RASPT2 was performed on top of each RASSCF calculation to account for the dynamical correlation; calculations have been performed setting the ionization-potential electron-

affinity shift[33] of 0.0 Hartree; to reduce problems with intruder states an imaginary shift[34] of 0.3 Hartree has been applied;

(5) Transition dipole moments between the sets of valence and core-hole states were computed through the RAS state interaction (SI) routine;

(6) The transition energies ω and the transition dipole moments TDM were used to simulate near-edge X-ray absorption spectra with the ground and first excited state ($n\pi^*$) as reference, denoted GS-NEXAFS and $n\pi^*$-NEXAFS, respectively. The stick spectrum was dressed by a Gaussian broadening, given by the equation

$$S_x - \mathrm{NEXAFS}(\omega) = \frac{1}{\sigma\sqrt{2\pi}} \sum_i |\mathrm{TMD}_{S_x \to i}|^2 \exp\left[\frac{-(\omega - \omega_{S_x \to i})^2}{2\sigma^2}\right] \quad (1)$$

where S_x represents either the GS or the $n\pi^*$ state, the sum runs over the core-hole excited state and a standard deviation of 0.4 eV (corresponding to a full-width-at-half-maximum broadening of $\sim$0.9 eV) was used.

Scalar relativistic effects have been included by using a second-order Douglas–Kroll–Hess Hamiltonian in combination with a relativistic atomic natural orbital basis set, ANO-RCC.[35] A triple-ζ basis function set augmented with two sets of d-functions was used for carbons and nitrogens, whereas an additional set of f-functions was used to improve the description of nitrogen, thus giving rise to ANO-RCC: N[4s3p2d1f], C[4s3p2d], H[2s1p]. A density-fitting approximation of the electron repulsion integrals has been used, known as Cholesky decomposition.[36]

Calculations were performed on a variety of azobenzene geometries:

• The *cis*- and *trans*-GS minima;

• Varying the three degrees of freedom of paramount importance for the *cis*- to *trans*-photoisomerization: torsion (CNNC), symmetric and asymmetric bending angles CNN/NNC:

– CNNC = 140° (CNN/NNC = 126°), CNNC = 120° (CNN/NNC = 124°) and CNNC = 100° (CNN/NNC = 122°);

– CNN/NNC = 114° (CNNC = 180°), CNN/NNC = 122° (CNNC = 180°) and CNN/NNC = 126° (CNNC = 170°).

– CNN = 112°/NNC = 116°, CNN = 112°/NNC = 124° and CNN = 112°/NNC = 142°, for a fixed value of CNNC = 180°.

• The conical intersections (CIs) between the ground and $n\pi^*$ state: the minimum energy CI, characterized by a central torsion CNNC = 95° and asymmetric bending angles CNN/NNC = 116°/146°, and a planar (CNNC = 180°) CI, characterized by large bending angles CNN/NNC = 150°/150°;

• Along the minimum energy path which connects the *trans*-azobenzene Franck–Condon point on the $n\pi^*$ state with the lowest $n\pi^*$/GS conical intersection.

The minima were optimized at the MP2/ANO-L-VDZP level, the minimum energy CI at the MS-2-RASPT2/SA-2-RASSCF(4, 9|0, 0|4, 7) level (employing PT2 numerical gradients). The key molecular modes were studied through rigid scans. The minimum energy path was taken from a recently performed three-dimensional rigid scan along the key modes performed by some of the present authors.[37] All calculations were performed in gas-phase with the OpenMolcas suite.[25]

3 Results

In this section we show our results for GS- and nπ*-NEXAFS spectra computed at the previously listed molecular geometries, and introduce a model capable of explaining the simulated data (summarized in Fig. 4). NEXAFS spectra are characterized by isolated features from resonant states below the core ionization edge of an element. These features are originated by transitions from the element's core orbital to unoccupied valence orbitals, *e.g.* a π* orbital. The intensity of such core-to-valence transitions is determined by the spatial overlap between the confined core and the valence orbital.[8,38]

In NEXAFS spectra from excited states, additional features may appear. In a single electron Hartree–Fock picture, an excited state can be described as an electron–hole pair in a formerly occupied and an unoccupied molecular orbital: the azobenzene ππ* state is mainly described by a removal of one electron from the highest occupied molecular orbital, which is then placed in the lowest unoccupied molecular orbitals, both with π symmetry; the azobenzene nπ* state is instead characterized by the filling of the same π* orbital, with an electron coming from the nitrogen lone pairs. The creation of such a hole in a formerly occupied valence orbital enables an additional NEXAFS resonance to be visualized when probing the (VIS/UV) excited system with an X-ray pulse.

The fact that the absorption cross-section of the various core-level transitions mainly depends on the spacial overlap between the starting and arrival orbitals makes it clear why the 1s → n transition from the strongly localized heteroatom 1s core to the electron hole of the nπ* state should appear brighter than the 1s → π transition from the same core to the more delocalized π orbital of a ππ* state. This idea was exploited by Wolf *et al.*[13] to show the internal conversion rate between the ππ* state (characterized by a weak 1s → π transition) to the nπ* state (with a much stronger 1s → n transition), performing time-resolved NEXAFS experiments at the thymine oxygen K-edge.

In what follows we will focus on nitrogen spectral signatures originated by the intense 1s → π* and 1s → n transitions. These fall approximately in the region between 395 and 400 eV. Core transitions to higher π* orbitals and virtual orbitals outside the active space are blue-shifted with respect to this window. Since these are generally a large number of low-intensity, overlapping signals, it is more difficult to extract information in that region of the spectrum. This was the reason, together with a reduced computational cost, why we limit ourselves to the computation of 15 core-level excitations in the active space of Fig. 1, and focus our analysis on the clean and informative signals of the 395–400 eV window.

3.1 NEXAFS on *cis*- and *trans*-azobenzene

GS-NEXAFS and nπ*-NEXAFS spectra computed at the optimized GS minima of *cis*- and *trans*-azobenzene are shown in Fig. 2. The gross features are summarized here: the presence of the intense 1s → π* transition in both the GS- and nπ*-NEXAFS spectra between 398–399 eV, and the appearance of the additional, red-shifted, 1s → n transition uniquely in the nπ*-NEXAFS spectrum around 396 eV. The weaker contributions observed above 400 eV are assigned to transitions into higher π* orbitals. The weak intensity is attributed to the fact that the higher lying π* orbitals are mainly localized on the phenyl moieties, effectively decreasing the

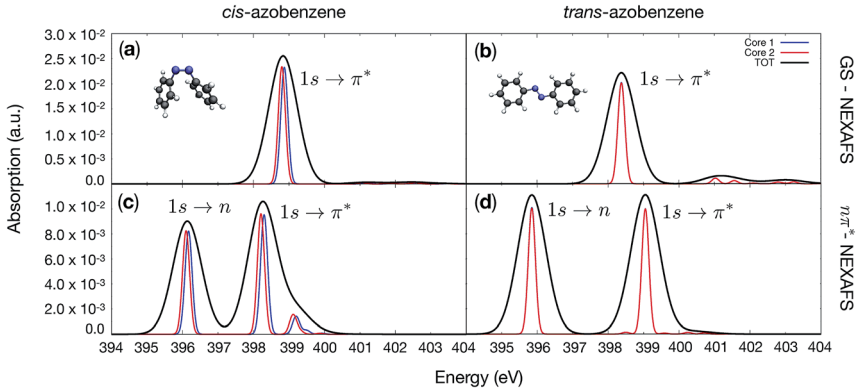

Fig. 2 NEXAFS spectra for *cis*-azobenzene (a and c) and *trans*-azobenzene (b and d). Color spectra are obtained with a Gaussian broadening of 0.1 eV and correspond to exciting cores c1 (blue) and c2 (red, see Fig. 1 for notation). The black spectrum represents the sum of the individual core spectra with a broadening of 0.4 eV. The molecular structure is also reported in the inset of (a) and (b). (a) and (b) show GS-NEXAFS, (c) and (d) show nπ*-NEXAFS of both species.

spatial overlap. A more detailed analysis of the transitions is reported in Table 1. Interestingly enough, from a qualitative point of view, the NEXAFS spectra for both geometries exhibit similar features in terms of peak positions, nature of the transition and intensity with spectral shifts of about 0.5 eV. Notably, the gap between the 1s → n and 1s → π* bands is larger by *ca.* 1 eV in *trans*-azobenzene with respect to the *cis*-form. We also note that the contributions from both nitrogens (c1 and c2) to the NEXAFS spectra are identical (blue and red bands in Fig. 2). This is related to the symmetry of these molecular structures, which makes the two core indistinguishable by definition. The slight splitting of the 1s → π* band observed in the *cis* NEXAFS spectra is an artifact of a strong state mixing of energetically close lying roots at the RASSCF level (see Table 1) leading to a pronounced artificial peak splitting. This mixing is largely corrected at the multi-state RASPT2 level, the results of which are plotted in Fig. 2.

These FC spectra can be compared to those reported recently by Ehlert and co-workers,[17] computed within the density functional theory framework, in combination with transition potential and ΔSCF methodology (TDDFT/ΔSCF). Focusing on the 395–400 eV spectral region, one observes that the GS-NEXAFS is characterized by the same intense 1s → π* transition blue-shifted by *ca.* 1.5 eV with respect to our calculations. Regarding the nπ*-NEXAFS, Ehlert and coworkers successfully predict the appearance of a red-shifted peak, associated with the 1s → n transition (again, slightly blue-shifted with respect to our results). Notably, the nπ*-NEXAFS of ref. 17 do not show the peak related to the 1s → π* transition, which is in contrast clearly visible in our simulations. The reason for this discrepancy could be found in the fact that TDDFT is essentially blind to doubly excited states, such as the one generated out of the nπ* state through the 1s → π* excitation. In multi-configuration wave function methods, instead, single and many electron excitations are described on an equal footing.

Table 1 Report of the properties of the main peaks observed in Fig. 2: configurations with the highest weight, weight, RASPT2 energies (in eV), and the module squared of the transition dipole moment (in a.u.^{2}). Configurations are labeled by occupation number of the three orbitals 1s, n, and π*

	cis-Azo					*trans*-Azo				
	Peak label	Main config.	Weight	Energy (PT2)	$\|TDM\|^2$	Peak label	Main config.	Weight	Energy (PT2)	$\|TDM\|^2$
GS-NEXAFS	—	$1s^{[1]}n^{[2]}\,\pi^{*[1]}$	0.90	398.9	5.82×10^{-3}	—	$1s^{[1]}n^{[2]}\,\pi^{*[1]}$	0.89	398.4	5.07×10^{-3}
nπ*-NEXAFS	—	$1s^{[1]}n^{[2]}\,\pi^{*[1]}$	0.90	396.2[a]	2.07×10^{-3}	—	$1s^{[1]}n^{[2]}\,\pi^{*[1]}$	0.89	395.9	2.53×10^{-3}
	—	$1s^{[1]}n^{[1]}\,\pi^{*[2]}$	0.67	398.3[a]	2.39×10^{-3}	—	$1s^{[1]}n^{[1]}\pi^{*[2]}$	0.90	399.1	2.46×10^{-3}
	—	$1s^{[1]}n^{[1]}\,\pi^{*[2]}$	0.36	399.2[a]	3.48×10^{-4}					

[a] These values are computed at the MS-RASPT2 level.

3.2 NEXAFS along key molecular modes

It has been demonstrated previously that the *cis–trans* isomerization in azobenzene can be described in terms of a few important coordinates, namely: the CNN/NNC bendings and the torsion around the central CNNC dihedral.[37,39,40] In Fig. 3 we show the effect of the motion along (1) symmetric CNN/NNC bending, (2) CNNC torsion and (3) asymmetric CNN/NNC bending on the simulated GS- and nπ*-NEXAFS spectra. In particular, we observe that:

(1) Symmetry-conserving variation of the CNN/NNC bending values does not affect the 1s → π* transition in both GS- and nπ*-NEXAFS. At the same time, the motion along this coordinate produces a clear blue-shift of the 1s → n transition in the nπ*-NEXAFS spectrum (bottom part of Fig. 3).

(2) *Vice versa*, the 1s → n transition is insensitive to motion along the CNNC torsion, which instead causes the 1s → π* peak to red-shift in both NEXAFS spectra from the FC geometries (CNNC values 0° and 180°) towards the 90° twisted geometry (central part of Fig. 3).

(3) Asymmetric variation of the CNN/NNC bending angles introduces a novel feature; namely, it breaks the symmetry thus making the two cores non-equivalent. As a consequence, core-specific signals appear which affect all signals (top part of Fig. 3). As expected, variation of the CNN/NNC bending values blue-shifts the 1s → n transitions; however, the c1 and c2 contributions are affected to a different extent, giving rise to a pronounced broadening of the peak when realistic peak broadening is applied. Similar peak broadening is observed

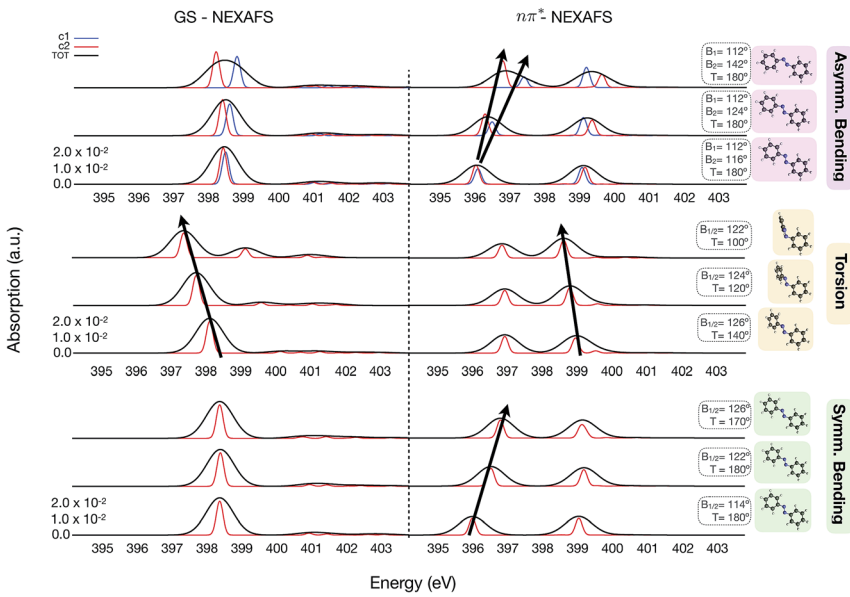

Fig. 3 Impact of geometrical distortions along key molecular modes on GS- and nπ*-NEXAFS spectra, namely symmetric CNN/NNC bending (bottom panel), CNNC torsion (middle panel) and asymmetric CNN/NNC bending (top panel). The spectral shifts of the peaks are highlighted by black arrows. Molecular structures with the corresponding values for torsion and bending angles are also shown (labels B_1 and B_2 refer to CNN and NNC bending respectively, while *T* stands for the CNNC torsion).

also for the 1s → π* transitions. Interestingly enough, the c1 signals always appear enframed by c2 signals.

3.3 Molecular orbital-based rationalization of the observed trends

In order to rationalize the observed signal trends along the specific modes, we build a simple model which involves only a limited number of orbitals, namely: the two nitrogen 1s core orbitals c1 and c2, their lone pair n (being the highest occupied molecular orbital), the π and the π* (which is the lowest unoccupied orbital) highlighted by the color boxes in Fig. 1. The model is reported in Fig. 4.

The model assumes that the energies of the core orbitals are not affected by the geometrical deformations as they are localized at the nitrogens. The spectral shifts observed in the NEXAFS spectra are, rather, understood as a function of the valence orbital energies, which exhibit mode-specific dependence. For example, the red-shift of the 1s → π* transition in both the GS- and nπ*-NEXAFS spectra along the torsional coordinate connecting the FC points of *cis*- and *trans*-azobenzene with the 90° twisted geometry (central part of Fig. 3) is a consequence of the associated stabilization of the π* orbital due to the decreasing anti-bonding character. Similarly, symmetry-conserving CNN/NNC bending deformations with respect to the nπ* equilibrium value of 126° increase the energy of the n orbital, due to increasing Coulomb repulsion of the lone pair electrons and the rest of the system. This effectively increases the core-n orbital band gap and induces a blue-shift of the core-n transition in the nπ*-NEXAFS spectrum.

In order to explain the band splitting in the case of asymmetric deformations, it is necessary to have a more in-depth look at the electronic structure of the core-

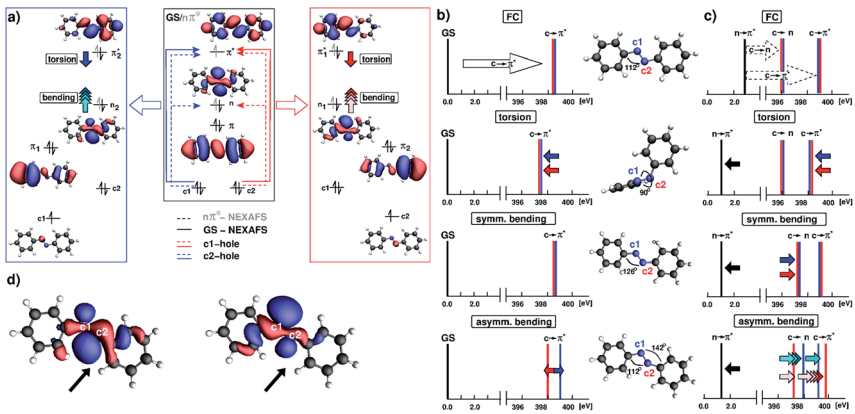

Fig. 4 Molecular orbital model used to rationalize the observed trends in the simulated NEXAFS spectra. (a) The central box shows the valence orbitals π, π* and the lone pair n and highlights possible core–valence transitions from either c1 or c2 (in blue and red) out of the GS and out of the nπ* state, giving rise to the GS- and nπ*-NEXAFS spectra, respectively. Side boxes show the localization effect on the valence orbitals which accompanies a core-excitation. (b and c) Schematic representation of the impact of geometrical distortions along key molecular modes on GS-NEXAFS (b) and on the nπ*-NEXAFS (c) with respect to the spectra in the Franck–Condon region (first row). A description of the model is outlined in Section 3.2. (d) Localization pattern of the lone pairs upon core-excitation of c1 (left) and c2 (right) in an asymmetrically distorted *trans*-azobenzene (CNN/NNC = 112°/142°).

hole states. The valence π orbitals of core-saturated azobenzene are delocalized over the entire molecule body giving rise to a strongly conjugated π-system, whereas the lone pair is localized on the central fragment. The removal of one electron from the 1s orbital of nitrogen upon core-excitation decreases dramatically the electronic shielding effect of the nuclear positive charge. As a consequence the electronegativity of the core-excited nitrogen increases and it withdraws electron density from the neighboring atoms. Mulliken charge analysis reveals that core-excited nitrogen accumulates nearly a unit negative charge, even if it has a core-hole. The enhanced electron-withdrawing effect of the core-excited center translates into lowering the energy of its atomic orbitals. For example, Fig. 4(a) shows how upon core-excitation the nitrogen p-type orbital decouples from the aromatic system, thus breaking the conjugation, and localizes on the core-excited center. The frontier lone pair, instead, localizes on the opposite center. In symmetric geometries one can expect to encounter symmetry-preserving orbitals due to the equivalence of the core-excited centers. However, in asymmetric geometries the localization is likely to dominate. The localization of the frontier lone pair during core-excitation in asymmetrically bent azobenzene leads to a non-uniform blue-shift of the 1s → n transitions (Fig. 4(c) bottom panel), as in one of the two localized lone pairs the Coulomb repulsion with the surroundings is stronger. This effect is demonstrated in Fig. 4(d) for an azobenzene having a pair of bending angles CNN/NNC = 112°/143°. As is evident, an electron pair in the frontier n orbital of the c1-hole system, localized predominantly on c2, is subjected to a strong repulsion with the neighbouring phenyl hydrogen. The repulsion is less pronounced for the frontier n orbital of the c2-hole system. Consequently, localizing the lone pair in the c1-hole (blue component in the c → π* and c → n dual peak in Fig. 4(b) and (c) bottom panel) requires more energy with respect to the c2-hole. The stronger repulsion to which the lone pair of the c1-hole is subjected makes a subsequent n → π* excitation energetically more favorable. This explains the inverted order of the blue and red components in the 1s → π* band of the nπ*-NEXAFS spectrum.

The introduced model is therefore capable of explaining the observed behaviours in the simulated spectra, in terms of stabilization and destabilization of the frontier orbitals π* and n, respectively, accompanied by localization in case of symmetry breaking.

3.4 NEXAFS signals at the conical intersections

In Fig. 5 we report NEXAFS spectra for two representative CIs between the ground and nπ* states: the asymmetrically bent minimum energy CI, characterized by a central torsion CNNC = 95° and a bending angle pair CNN/NNC = 116°/146° (Fig. 5(a) and (c)) and a symmetry-conserving planar (CNNC = 180°) CI, characterized by large bending angles CNN/NNC = 150°/150° (Fig. 5(b) and (d)). We avoid the notation GS and nπ* when dealing with CIs and use, instead, the notation closed-shell and open-shell, as both configurations are virtually degenerate at the crossing and change energetic order along various degrees of freedom. A detailed analysis of the transitions at the CIs is given in Table 2.

We note the pronounced difference between the closed-shell NEXAFS spectra for both species (Fig. 5(a) and (b)). The spectrum of the asymmetric CI shows two clear peaks, both associated with a 1s → π* transition, either from c1 or c2. As

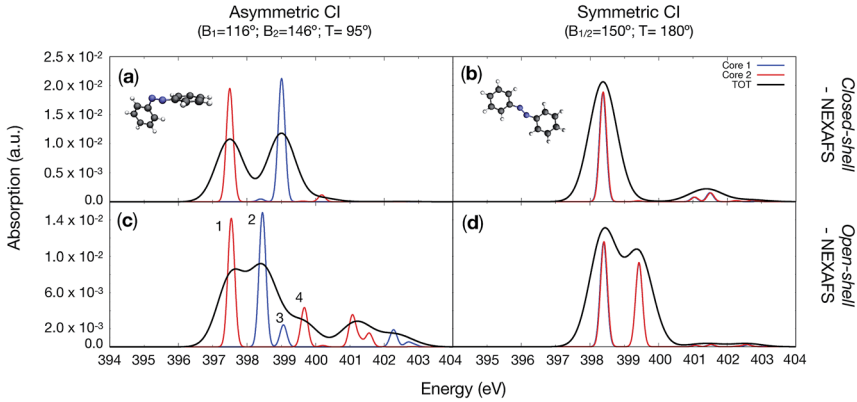

Fig. 5 GS- and nπ*-NEXAFS spectra of the symmetry-breaking minimum energy CI with central torsion CNNC = 95° (a and c) and of a symmetry-conserving CI accessible from the *trans*-side characterized by a large CNN/NNC bending value of 150° (b and d). The molecular structure is also reported in the inset of (a) and (b). Color spectra are obtained with a broadening of 0.1 eV and correspond to exciting cores c1 (blue) and c2 (red, see Fig. 1 for notation). The black spectrum represents the sum of the individual core spectra with a broadening of 0.4 eV. (a) and (b) show closed-shell-NEXAFS, (c) and (d) show open-shell-NEXAFS of both species.

elucidated in the previous section, the non-equivalence of the two cores induces a splitting of the 1s → π* band which for large asymmetric deformations could reach values as large as 1.5 eV, well beyond the FWHM width of the peak. The closed-shell spectrum of the symmetric CI is characterized by a single peak which exhibits virtually no shift with respect to the GS-NEXAFS at the FC point. This observation is in agreement with the notion that the GS/closed-shell NEXAFS spectrum does not change along the bending degree of freedom (bottom part of Fig. 3).

The realistically broadened open-shell NEXAFS spectra of both species have similar line shapes (Fig. 5(c) and (d)), characterized by a single broad band with fine structure. However, the underlying transitions are rather different. The main contribution to the spectrum of the asymmetric CI arises from the splitting of the 1s → n transitions, whereas the 1s → π* signals are less intense. Remarkably, the repulsion of the doubly occupied lone pair in the c1-hole state (peak 2 in Fig. 5(c)) becomes so large due to the strong asymmetric deformation (Fig. 4(d)) that promoting an electron out of the n orbital into the π* is done at almost no cost (peak 3 in Fig. 5(c) blue-shifted by 0.5 eV). The broadening of the open-shell spectrum of the symmetric CI is the result of the strong destabilization of the n orbital along the bending coordinate by about 2.5 eV with respect to the FC spectrum of the *trans*-form (Fig. 2(d)), which causes the blue-shift of the 1s → n transition from 396 eV to 398.5 eV, in agreement with our model (Fig. 4(c)).

On the basis of the previous analysis, we can conclude that conical intersections exhibit a characteristic spectral fingerprint which may be used to track a wave packet evolving on the nπ* state potential energy surface when it approaches the crossing seam. This signature is a single broad band spanning the entire 397–400 eV spectral window and exhibiting a fine structure which

Table 2 Report of the properties of the main peaks observed in Fig. 5: configurations with the highest weight, weight, RASPT2 energies (in eV), and the module squared of the transition dipole moment (in a.u.^{2}). Configurations are labeled by occupation number of the three orbitals 1s, n, and π^*

	Peak label[a]	Main config.	Weight	Energy (PT2)	$\lvert TDM\rvert^2$	Peak label[a]	Main config.	weight	Energy (PT2)	$\lvert TDM\rvert^2$
Asymmetric CI (c1)						**Asymmetric CI (c2)**				
Cl.-shell NEXAFS	—	$1s^{[1]}n^{[2]}\,\pi^{*[1]}$	0.78	399.0	5.32×10^{-3}	—	$1s^{[1]}n^{[2]}\,\pi^{*[1]}$	0.89	397.5	4.89×10^{-3}
Op.-shell NEXAFS	2	$1s^{[1]}n^{[2]}\,\pi^{*[1]}$	0.83	398.5	3.71×10^{-3}	1	$1s^{[1]}n^{[2]}\,\pi^{*[1]}$	0.89	397.5	3.55×10^{-3}
	3	$1s^{[1]}n^{[1]}\,\pi^{*[2]}$	0.78	399.1	6.09×10^{-4}	4	$1s^{[1]}n^{[1]}\,\pi^{*[2]}$	0.78	399.7	1.09×10^{-3}
Symmetric CI										
Cl.-shell NEXAFS	—	$1s^{[1]}n^{[2]}\,\pi^{*[1]}$	0.89	398.4	4.68×10^{-3}					
Op.-shell NEXAFS	—	$1s^{[1]}n^{[2]}\,\pi^{*[1]}$	0.89	398.4	2.88×10^{-3}					
	—	$1s^{[1]}n^{[1]}\,\pi^{*[2]}$	0.90	399.4	2.31×10^{-3}					

[a] The peak labels refer to those of Fig. 5.

originates either from the merging of the 1s → n and 1s → π* bands, clearly separated in the FC region, into a single broad peak in the open-shell NEXAFS (symmetric CI), or by the core splitting of the 1s → n transition, with minor contributions from the 1s → π* transitions (asymmetric CI). The asymmetric CI seam exhibits another characteristic signature, a double-peak structure of its closed-shell spectrum, otherwise dominated by a single peak.

3.5 Minimum energy path

After discussing the dependence of the NEXAFS spectra on the geometrical deformations along key molecular modes, and after becoming acquainted with the characteristic spectral features of the crossing region, we are now in a position to apply optical-pump NEXAFS-probe spectroscopy to track the photo-induced *trans*- to *cis*-isomerization. A comprehensive non-adiabatic dynamics is out of the scope of the present study, which focuses only on the spectral dynamics along the MEP connecting the FC region of the *trans*-form with the minimum energy CI. Fig. 6(b) and (c) show the excited state profiles in the coordinate space of torsion and symmetric bending angles (c), as well as in the coordinate space of both bending angles (b) together with the MEP (the thick colored line which connects the points). Fig. 6(a) reports a sequence of NEXAFS spectra simulated along a few selected structures along the MEP. Upon photo-excitation, azobenzene exhibits a gradient directed along the symmetric bending coordinate which widens the CNN/NNC angles, a deformation associated with a blue-shift of the 1s → n peak in the nπ* spectrum. Molecular dynamics simulations have revealed that the initial motion along the symmetric bending coordinate explores a range of bending angle values of around ~30/40° and remains coherent for several oscillation periods.[37] This would translate into an oscillatory 1s → n spectral dynamics

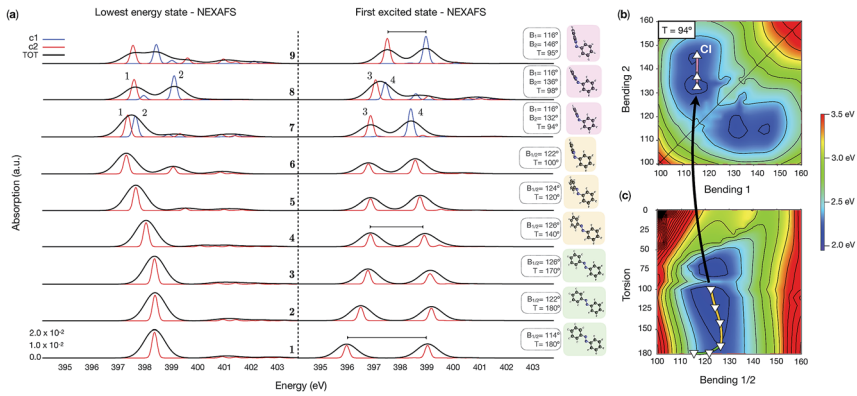

Fig. 6 (a) Lowest energy state and first excited state NEXAFS spectra along the minimum energy path (MEP) on the potential energy surface of the nπ* state from the Franck–Condon point of *trans*-azobenzene towards the asymmetric CI. The path itself is visualized as heat maps in the coordinate subspace of CNNC torsion and symmetric CNN/NNC bending (b) and in the subspace of both bendings at a fixed torsion $T = 94°$ (c). The maps are plotted using MS-2-RASPT2/SA-2-RASSCF(4, 9|0, 0|4, 7) nπ* energies from a rigid scan with the energy of the GS *trans*-minimum set as zero point reference.[37] The first six spectra (from the bottom), and the last one, have been already reported in Fig. 3 and 5, respectively.

Table 3 Report of the properties of the main peaks observed in Fig. 6: configurations with the highest weight, RASSCF and RASPT2 energies (in eV), and the module squared of the transition dipole moment (in a.u.^{2}). The orbital assignment at ~90° (MEP 7 and 8) is complicated by the observed mixing of n and π* orbitals; therefore, it was performed according to the maximal overlap with reference orbitals (the clean n and π* orbitals of MEP 1–6)

	Peak label[a]	Main config.	Weight	Energy (PT2)	$\|TDM\|^2$	Peak label[a]	Main config.	Weight	Energy (PT2)	$\|TDM\|^2$
MEP 1						**MEP 2**				
GS-NEXAFS	—	$1s^{[1]}n^{[2]}\,\pi^{*[1]}$	0.89	398.4	4.98×10^{-3}	—	$1s^{[1]}n^{[2]}\,\pi^{*[1]}$	0.88	398.4	4.97×10^{-3}
nπ*-NEXAFS	—	$1s^{[1]}n^{[2]}\,\pi^{*[1]}$	0.89	395.9	2.46×10^{-3}	—	$1s^{[1]}n^{[2]}\,\pi^{*[1]}$	0.88	396.4	2.64×10^{-3}
	—	$1s^{[1]}n^{[1]}\,\pi^{*[2]}$	0.90	399.1	2.42×10^{-3}	—	$1s^{[1]}n^{[1]}\,\pi^{*[2]}$	0.90	399.2	2.41×10^{-3}
MEP 3						**MEP 4**				
GS-NEXAFS	—	$1s^{[1]}n^{[2]}\,\pi^{*[1]}$	0.88	398.4	4.96×10^{-3}	—	$1s^{[1]}n^{[2]}\,\pi^{*[1]}$	0.88	398.0	4.68×10^{-3}
nπ*-NEXAFS	—	$1s^{[1]}n^{[2]}\,\pi^{*[1]}$	0.88	396.7	2.67×10^{-3}	—	$1s^{[1]}n^{[2]}\,\pi^{*[1]}$	0.88	396.8	2.46×10^{-3}
	—	$1s^{[1]}n^{[1]}\,\pi^{*[2]}$	0.71	399.1	1.61×10^{-3}	—	$1s^{[1]}n^{[1]}\,\pi^{*[2]}$	0.64	398.9	2.23×10^{-3}
MEP 5						**MEP 6**				
GS-NEXAFS	—	$1s^{[1]}n^{[2]}\,\pi^{*[1]}$	0.89	397.7	4.44×10^{-3}	—	$1s^{[1]}n^{[2]}\,\pi^{*[1]}$	0.89	397.3[b]	3.65×10^{-3}
						—	$1s^{[1]}n^{[1]}\,\pi^{*[2]}$	0.84	399.1[b]	1.33×10^{-3}
nπ*-NEXAFS	—	$1s^{[1]}n^{[2]}\,\pi^{*[1]}$	0.89	396.8	2.21×10^{-3}	—	$1s^{[1]}n^{[2]}\,\pi^{*[1]}$	0.89	396.8[b]	1.93×10^{-3}
	—	$1s^{[1]}n^{[1]}\,\pi^{*[2]}$	0.72	398.8	2.60×10^{-3}	—	$1s^{[1]}n^{[1]}\pi^{*[2]}$	0.84	398.6[b]	2.65×10^{-3}
MEP 7 (core 1)						**MEP 7 (core 2)**				
Op.-shell NEXAFS	2	$1s^{[1]}n^{[2]}\pi^{*[1]}$	0.86	397.7	4.09×10^{-3}	1	$1s^{[1]}n^{[1]}\pi^{*[2]}$	0.89	397.4	4.25×10^{-3}
Cl.-shell NEXAFS	4	$1s^{[1]}n^{[1]}\pi^{*[2]}$	0.87	398.5	5.45×10^{-3}	3	$1s^{[1]}n^{[1]}\pi^{*[2]}$	0.89	396.9	4.11×10^{-3}
MEP 8 (core 1)						**MEP 8 (core 2)**				
Cl.-shell NEXAFS	2	$1s^{[1]}n^{[1]}\pi^{*[2]}$	0.79	399.1[b]	4.68×10^{-3}	1	$1s^{[1]}n^{[1]}\pi^{*[2]}$	0.89	397.5[b]	3.93×10^{-3}
Op.-shell NEXAFS	4	$1s^{[1]}n^{[1]}\pi^{*[2]}$	0.89	397.4[b]	3.41×10^{-3}	3	$1s^{[1]}n^{[1]}\pi^{*[2]}$	0.89	397.0[b]	3.88×10^{-3}

[a] The peak labels refer to those of Fig. 6. [b] These values are obtained after the MSPT2 unmixing of the first three valence roots.

between 396 eV and 398 eV. Gradually, the energy is distributed into a motion along the flat torsional coordinate, thereby reducing the amplitude of the bending and destroying the coherence (*i.e.* breaking the symmetry). This process is associated with a red-shift of the 1s → π* transition. The loss of coherence with respect to the bending coordinate is expected to introduce a slight broadening of the peaks. Furthermore, with approaching the region of 90° torsion, the gap between the 1s → n and the 1s → π* peaks will diminish to about 1–1.5 eV. In the region of 90° torsion, azobenzene becomes subject to a gradient towards strong asymmetric distortion along the bending coordinate towards the CI seam. As seen in Fig. 5(a), this would induce a merging and broadening of the transient absorption signal. In this region the order of the states can swap, causing a sudden change of the observed signals. Upon decay to the GS and ultrafast leaving of the crossing region, our simulations suggest the decrease of signal intensity in the 400 eV spectral window. Instead, the oscillatory motion of the GS wave packet along the torsional degree of freedom would translate into an oscillatory 1s → π* spectral dynamics between 397 eV and 398.5 eV. However, this feature might be obscured by the considerable broadening expected due to the vibrational dynamics along the coordinate exhibiting very different values for CNN and NNC bending angles. A detailed analysis of the transitions along the MEP is also reported in Table 3.

4 Conclusion

We have shown here how time-resolved NEXAFS can be applied to study transient dynamics of UV-excited molecules, as its signals are sensitive to specific geometrical changes along the reactive coordinates.

The main results here reported are the following: (i) large geometrical deformations do not necessarily translate into large differences in the NEXAFS spectra, which are instead sensitive to displacements along coordinates which affect the valence orbitals of the bright core-to-valence transitions; (ii) the relevant coordinates, which describe the isomerization dynamics on the nπ* state provide, respectively: a blue shift of the 1s → n transition (symmetric bending), a core specific blue-shift of the signals accompanied by a pronounced broadening (asymmetric bending), and a red-shift of the 1s → π* transition (torsion), as summarized in Fig. 3.

The dynamics along the minimum energy path (Fig. 6), characterized by the following evolution along symmetric bending, torsion, and asymmetric bending, leads to the progressive merging of the 1s → π* and 1s → n signals, which reach the maximal overlap in the vicinity of the conical intersection seam. This feature promises a way to spot movement towards, and passage through, the crossing seam in transient absorption experiments. We note that significant broadening of the bands due to the ultrashort core-to-valence state lifetime does not impair the analysis.

We remark on the fact that, in the present contribution, we focused on the analysis of the signals of a single molecule at different geometries along the MEP, while an average over an ensemble of trajectories is necessary to simulate a realistic spectrum. This averaging over many trajectories translates into an averaging of signals coming from different regions of the PES, and may therefore result in a partial obscuring of some of the features. Furthermore, as in real experiments

the optical pump pulse excites only a fraction of the molecules in the sample, NEXAFS spectra record a superposition of the excited state (minor fraction) and the ground state (major fraction) absorption spectra. This requires the difference in the GS- and ES-NEXAFS spectra to be sufficiently large to be detected, as is the case with the 1s → n transition. Therefore, our analysis suggests that the best suited molecular targets for X-ray mapping should be organic molecules containing heteroatoms with electron lone pairs (like nucleobases, amino acids, and azoswitches) which are characterized by a coherent ballistic motion of a compact wave packet from the FC point to the CI region.

Conflicts of interest

There are no conflicts to declare.

Acknowledgements

M. G., F. S., A. N. and S. M. acknowledge support from the Chemical Sciences, Geosciences, and Bio-Sciences Division, Office of Basic Energy Sciences, Office of Science, U.S. Department of Energy, through award No. DE-SC0019484.

References

1 W. Ackermann, G. Asova, V. Ayvazyan, A. Azima, N. Baboi, J. Bähr, V. Balandin, B. Beutner, A. Brandt, A. Bolzmann, R. Brinkmann, O. I. Brovko, M. Castellano, P. Castro, L. Catani, E. Chiadroni, S. Choroba, A. Cianchi, J. T. Costello, D. Cubaynes, J. Dardis, W. Decking, H. Delsim-Hashemi, A. Delserieys, G. D. Pirro, M. Dohlus, S. Düsterer, A. Eckhardt, H. T. Edwards, B. Faatz, J. Feldhaus, K. Flöttmann, J. Frisch, L. Fröhlich, T. Garvey, U. Gensch, C. Gerth, M. Görler, N. Golubeva, H.-J. Grabosch, M. Grecki, O. Grimm, K. Hacker, U. Hahn, J. H. Han, K. Honkavaara, T. Hott, M. Hüning, Y. Ivanisenko, E. Jaeschke, W. Jalmuzna, T. Jezynski, R. Kammering, V. Katalev, K. Kavanagh, E. T. Kennedy, S. Khodyachykh, K. Klose, V. Kocharyan, M. Körfer, M. Kollewe, W. Koprek, S. Korepanov, D. Kostin, M. Krassilnikov, G. Kube, M. Kuhlmann, C. L. S. Lewis, L. Lilje, T. Limberg, D. Lipka, F. Löhl, H. Luna, M. Luong, M. Martins, M. Meyer, P. Michelato, V. Miltchev, W. D. Möller, L. Monaco, W. F. O. Müller, O. Napieralski, O. Napoly, P. Nicolosi, D. Nölle, T. Nuñez, A. Oppelt, C. Pagani, R. Paparella, N. Pchalek, J. Pedregosa-Gutierrez, B. Petersen, B. Petrosyan, G. Petrosyan, L. Petrosyan, J. Pflüger, E. Plönjes, L. Poletto, K. Pozniak, E. Prat, D. Proch, P. Pucyk, P. Radcliffe, H. Redlin, K. Rehlich, M. Richter, M. Roehrs, J. Roensch, R. Romaniuk, M. Ross, J. Rossbach, V. Rybnikov, M. Sachwitz, E. L. Saldin, W. Sandner, H. Schlarb, B. Schmidt, M. Schmitz, P. Schmüser, J. R. Schneider, E. A. Schneidmiller, S. Schnepp, S. Schreiber, M. Seidel, D. Sertore, A. V. Shabunov, C. Simon, S. Simrock, E. Sombrowski, A. A. Sorokin, P. Spanknebel, R. Spesyvtsev, L. Staykov, B. Steffen, F. Stephan, F. Stulle, H. Thom, K. Tiedtke, M. Tischer, S. Toleikis, R. Treusch, D. Trines, I. Tsakov, E. Vogel, T. Weiland, H. Weise, M. Wellhöfer, M. Wendt, I. Will, A. Winter, K. Wittenburg, W. Wurth,

P. Yeates, M. V. Yurkov, I. Zagorodnov and K. Zapfe, *Nat. Photonics*, 2007, **1**, 336–342.

2 P. Emma, R. Akre, J. Arthur, R. Bionta, C. Bostedt, J. Bozek, A. Brachmann, P. Bucksbaum, R. Coffee, F.-J. Decker, Y. Ding, D. Dowell, S. Edstrom, A. Fisher, J. Frisch, S. Gilevich, J. Hastings, G. Hays, P. Hering, Z. Huang, R. Iverson, H. Loos, M. Messerschmidt, A. Miahnahri, S. Moeller, H.-D. Nuhn, G. Pile, D. Ratner, J. Rzepiela, D. Schultz, T. Smith, P. Stefan, H. Tompkins, J. Turner, J. Welch, W. White, J. Wu, G. Yocky and J. Galayda, *Nat. Photonics*, 2010, **4**, 641–647.

3 T. Ishikawa, H. Aoyagi, T. Asaka, Y. Asano, N. Azumi, T. Bizen, H. Ego, K. Fukami, T. Fukui, Y. Furukawa, S. Goto, H. Hanaki, T. Hara, T. Hasegawa, T. Hatsui, A. Higashiya, T. Hirono, N. Hosoda, M. Ishii, T. Inagaki, Y. Inubushi, T. Itoga, Y. Joti, M. Kago, T. Kameshima, H. Kimura, Y. Kirihara, A. Kiyomichi, T. Kobayashi, C. Kondo, T. Kudo, H. Maesaka, X. M. Maréchal, T. Masuda, S. Matsubara, T. Matsumoto, T. Matsushita, S. Matsui, M. Nagasono, N. Nariyama, H. Ohashi, T. Ohata, T. Ohshima, S. Ono, Y. Otake, C. Saji, T. Sakurai, T. Sato, K. Sawada, T. Seike, K. Shirasawa, T. Sugimoto, S. Suzuki, S. Takahashi, H. Takebe, K. Takeshita, K. Tamasaku, H. Tanaka, R. Tanaka, T. Tanaka, T. Togashi, K. Togawa, A. Tokuhisa, H. Tomizawa, K. Tono, S. Wu, M. Yabashi, M. Yamaga, A. Yamashita, K. Yanagida, C. Zhang, T. Shintake, H. Kitamura and N. Kumagai, *Nat. Photonics*, 2012, **6**, 540–544.

4 M. Kowalewski, B. P. Fingerhut, K. E. Dorfman, K. Bennett and S. Mukamel, *Chem. Rev.*, 2017, **117**, 12165–12226.

5 M. Kowalewski, K. Bennett and S. Mukamel, *Struct. Dyn.*, 2017, **4**, 054101.

6 J. R. Rouxel, Y. Zhang and S. Mukamel, *Chem. Sci.*, 2019, **10**, 898–908.

7 M. Gühr, *Synchrotron Radiat. News*, 2016, **29**, 8–12.

8 J. Stöhr, *NEXAFS Spectroscopy*, Springer Berlin Heidelberg, 1992.

9 *X-Ray Absorption and X-Ray Emission Spectroscopy*, ed. J. A. V. Bokhoven and C. Lamberti, John Wiley & Sons, Ltd, 2016.

10 C. Bressler and M. Chergui, *Annu. Rev. Phys. Chem.*, 2010, **61**, 263–282.

11 P. Wernet, K. Kunnus, I. Josefsson, I. Rajkovic, W. Quevedo, M. Beye, S. Schreck, S. Grübel, M. Scholz, D. Nordlund, W. Zhang, R. W. Hartsock, W. F. Schlotter, J. J. Turner, B. Kennedy, F. Hennies, F. M. F. de Groot, K. J. Gaffney, S. Techert, M. Odelius and A. Föhlisch, *Nature*, 2015, **520**, 78–81.

12 A. R. Attar, A. Bhattacherjee, C. D. Pemmaraju, K. Schnorr, K. D. Closser, D. Prendergast and S. R. Leone, *Science*, 2017, **356**, 54–59.

13 T. J. A. Wolf, R. H. Myhre, J. P. Cryan, S. Coriani, R. J. Squibb, A. Battistoni, N. Berrah, C. Bostedt, P. Bucksbaum, G. Coslovich, R. Feifel, K. J. Gaffney, J. Grilj, T. J. Martinez, S. Miyabe, S. P. Moeller, M. Mucke, A. Natan, R. Obaid, T. Osipov, O. Plekan, S. Wang, H. Koch and M. Gühr, *Nat. Commun.*, 2017, **8**, 29.

14 P. A. Malmqvist, A. Rendell and B. O. Roos, *J. Phys. Chem.*, 1990, **94**, 5477–5482.

15 K. Andersson, P. A. Malmqvist, B. O. Roos, A. J. Sadlej and K. Wolinski, *J. Phys. Chem.*, 1990, **94**, 5483–5488.

16 V. Sauri, L. S. Andres, A. R. M. Shahi, L. Gagliardi, S. Vancoillie and K. Pierloot, *J. Chem. Theory Comput.*, 2011, **7**, 153.

17 C. Ehlert, M. Gühr and P. Saalfrank, *J. Chem. Phys.*, 2018, **149**, 144112.

18 D. Polli, P. Altoè, O. Weingart, K. M. Spillane, C. Manzoni, D. Brida, G. Tomasello, G. Orlandi, P. Kukura, R. A. Mathies, M. Garavelli and G. Cerullo, *Nature*, 2010, **467**, 440–443.
19 B. O. Roos, *Ab Initio Methods in Quantum Chemistry: Part II*, Wiley, Chichester, UK, 1987.
20 B. O. Roos, P. R. Taylor and P. E. M. Siegbahn, *Chem. Phys.*, 1980, **48**, 157.
21 D. Roca-Sanjuán, F. Aquilante and R. Lindh, *Wiley Interdiscip. Rev.: Comput. Mol. Sci.*, 2011, **2**, 585–603.
22 J. Norell, R. M. Jay, M. Hantschmann, S. Eckert, M. Guo, K. J. Gaffney, P. Wernet, M. Lundberg, A. Föhlisch and M. Odelius, *Phys. Chem. Chem. Phys.*, 2018, **20**, 7243–7253.
23 I. Josefsson, K. Kunnus, S. Schreck, A. Föhlisch, F. de Groot, P. Wernet and M. Odelius, *J. Phys. Chem. Lett.*, 2012, **3**, 3565–3570.
24 W. Hua, S. Oesterling, J. D. Biggs, Y. Zhang, H. Ando, R. de Vivie-Riedle, B. P. Fingerhut and S. Mukamel, *Struct. Dyn.*, 2015, **3**, 023601.
25 F. Aquilante, J. Autschbach, R. K. Carlson, L. F. Chibotaru, M. G. Delcey, L. D. Vico, I. F. Galván, N. Ferré, L. M. Frutos, L. Gagliardi, M. Garavelli, A. Giussani, C. E. Hoyer, G. L. Manni, H. Lischka, D. Ma, P. Å. Malmqvist, T. Müller, A. Nenov, M. Olivucci, T. B. Pedersen, D. Peng, F. Plasser, B. Pritchard, M. Reiher, I. Rivalta, I. Schapiro, J. Segarra-Martí, M. Stenrup, D. G. Truhlar, L. Ungur, A. Valentini, S. Vancoillie, V. Veryazov, V. P. Vysotskiy, O. Weingart, F. Zapata and R. Lindh, *J. Comput. Chem.*, 2015, **37**, 506–541.
26 M. Lundberg and M. G. Delcey, *Transition Metals in Coordination Environments*, Springer International Publishing, 2019.
27 T. Fleig, J. Olsen and L. Visscher, *J. Chem. Phys.*, 2003, **119**, 2963–2971.
28 D. Ma, G. L. Manni and L. Gagliardi, *J. Chem. Phys.*, 2011, **135**, 044128.
29 M. Guo, L. K. Sørensen, M. G. Delcey, R. V. Pinjari and M. Lundberg, *Phys. Chem. Chem. Phys.*, 2016, **18**, 3250–3259.
30 E. Ertan, V. Savchenko, N. Ignatova, V. V. da Cruz, R. C. Couto, S. Eckert, M. Fondell, M. Dantz, f. A. P. Brian Kennedy, T. Schmitt, A. Frölich, F. GelâĂŹmukhanov, M. Odelius and V. Kimberg, *Phys. Chem. Chem. Phys.*, 2018, **20**, 14384.
31 W. Humphrey, A. Dalke and K. Schulten, *J. Mol. Graphics*, 1996, **14**, 33–38.
32 J. Stone, M.Sc. thesis, Computer Science Department, University of Missouri-Rolla, 1998.
33 G. Ghigo, B. O. Roos and P. Malmqvist, *Chem. Phys. Lett.*, 2004, **396**, 142–149.
34 N. Forsberg and P. Malmqvist, *Chem. Phys. Lett.*, 1997, **274**, 196–204.
35 B. O. Roos, V. Veryazov and P.-O. Widmark, *Theor. Chem. Acc.*, 2004, **11**, 345.
36 F. Aquilante, T. B. Pedersen and R. Lindh, *Theor. Chem. Acc.*, 2009, **124**, 1.
37 F. Aleotti, L. Soprani, A. Nenov, R. Berardi, C. Zannoni and M. Garavelli, 2019, submitted.
38 R. Manne, *J. Chem. Phys.*, 1970, **52**, 5733–5739.
39 J. Casellas, M. J. Bearpark and M. Reguero, *ChemPhysChem*, 2016, **17**, 3068–3079.
40 A. Nenov, R. Borrego-Varillas, A. Oriana, L. Ganzer, F. Segatta, I. Conti, J. Segarra-Marti, J. Omachi, M. Dapor, S. Taioli, C. Manzoni, S. Mukamel, G. Cerullo and M. Garavelli, *J. Phys. Chem. Lett.*, 2018, **9**, 1534–1541.